

1 **HRLT: A high-resolution (1 day, 1 km) and long-term**
2 **(1961–2019) gridded dataset for surface temperature**
3 **and precipitation across China**

4 Rongzhu Qin, Zeyu Zhao, Jia Xu, Jian-Sheng Ye, Feng-min Li, Feng Zhang*

5 State Key Laboratory of Herbage Improvement and Grassland Agro-ecosystems, College of
6 Ecology, Lanzhou University, Lanzhou, 730000, China

7 * Corresponding author: Feng Zhang

8 Tel.: +86 13919274617

9 Fax: +86 09318912561

10 E-mail: zhangfeng@lzu.edu.cn

11 Address: College of Ecology, Lanzhou University, 222 Tian Shui South Road, Lanzhou, 730000,
12 China

13

14

15

16

17

18

19

20

21

22

Abstract

Accurate long-term temperature and precipitation estimates at high spatial and temporal resolutions are vital for a wide variety of climatological studies. We have produced a new, publicly available, daily, gridded maximum temperature, minimum temperature, and precipitation dataset for China with a high spatial resolution of 1 km and over a long-term period (1961 to 2019). It has been named the HRLT and the dataset is publicly available at <https://doi.org/10.1594/PANGAEA.941329> (Qin and Zhang, 2022). In this study, the daily gridded data were interpolated using comprehensive statistical analyses, which included machine learning methods, the generalized additive model, and thin plate splines. It was based on the $0.5^\circ \times 0.5^\circ$ gridded dataset from the China Meteorological Administration, together with covariates for elevation, aspect, slope, topographic wetness index, latitude, and longitude. The accuracy of the HRLT daily dataset was assessed using observation data from meteorological stations across China. The maximum and minimum temperature estimates were more accurate than the precipitation estimates. For maximum temperature, the mean absolute error (MAE), root mean square error (RMSE), Pearson's correlation coefficient (Cor), coefficient of determination after adjustment (R^2), and Nash-Sutcliffe modeling efficiency (NSE) were 1.07 °C, 1.62 °C, 0.99, 0.98, and 0.98, respectively. For minimum temperature, the MAE, RMSE, Cor, R^2 , and NSE were 1.08 °C, 1.53 °C, 0.99, 0.99, and 0.99, respectively. For precipitation, the MAE, RMSE, Cor, R^2 , and NSE were 1.30 mm, 4.78 mm, 0.84, 0.71, and 0.70, respectively. The accuracy of the HRLT was compared to those of the other three existing datasets and its accuracy was either greater than the others, especially for precipitation, or comparable in accuracy, but with higher spatial resolution or over a longer time period. In summary, the HRLT dataset, which has a high spatial resolution, covers a longer period of time and has reliable accuracy.

45 **1 Introduction**

46 Climate change has led to an increase in the frequency and severity of extreme temperature
47 and precipitation events (Myhre et al., 2019), and these events have affected vegetation growth (Xu
48 et al., 2019), especially crop growth (Rao et al., 2015; Li et al., 2019b; Lu et al., 2018; Lobell et al.,
49 2011; Lesk et al., 2016). Thus, long-term and accurate daily maximum temperature, minimum
50 temperature, and precipitation data are important when attempting to reveal the mechanism
51 underlying the effects of extreme climate on plants, predicting disasters (such as drought, frost, and
52 floods), and for agricultural and forestry management. Although the meteorological observation
53 network makes better use of the data from meteorological stations (Merino et al., 2014; Yang et al.,
54 2014), there is a tradeoff between large spatial scale and the high density of stations in the
55 meteorological observation network. Moreover, the installation and maintenance of meteorological
56 stations are challenging in harsh areas (Hartl et al., 2020). Daily and gridded meteorological datasets
57 are also essential inputs for many models related to terrestrial, hydrological, and ecological systems
58 (Iizumi et al., 2017; Wang et al., 2018; Zhang et al., 2018; Lee et al., 2019). High-resolution, long-
59 term, and accurate gridded datasets can help improve the performance of these models.

60 Researchers have previously used interpolation methods, such as inverse distance weighting,
61 kriging, and regression analysis, to produce gridded meteorological data (Brinckmann et al., 2016;
62 Herrera et al., 2019; Schamm et al., 2014). However, the accuracy of these interpolation results is
63 limited by the density of the meteorological stations. In recent years, artificial intelligence, machine
64 learning methods, such as random forest (Chen et al., 2021; Sekulić et al., 2021); artificial neural
65 networks (Sadeghi et al., 2021), and support vector machines (He et al., 2021) have been gradually

66 and widely applied to meteorological data estimation. Therefore, comprehensive statistical analyses
67 using machine learning and traditional interpolation, such as thin-plate-smoothing splines, are
68 feasible and reliable methods that can be used to estimate meteorological data.

69 At present, only a few research institutes in China are developing meteorological datasets for
70 temperature and precipitation with high spatial and temporal resolutions. Among them, Beijing
71 Normal University has produced meteorological datasets for 1958–2010 with a resolution of 1 km,
72 but the latest data is not available (Li et al., 2014). The China Meteorological Administration is also
73 developing the CMA Land Data Assimilation System product (Shi et al., 2011) and Tsinghua
74 University has published a driving dataset from 1979 to 2018 with a resolution of 0.1° over China
75 (He et al., 2020).

76 We present a new high-resolution daily gridded maximum temperature, minimum temperature,
77 and precipitation dataset for China (HRLT) with a spatial resolution of 1×1 km for the period 1961
78 to 2019. We created the HRLT dataset using comprehensive statistical analyses, which included
79 machine learning, the generalized additive model and thin plate splines. It uses the $0.5^\circ \times 0.5^\circ$
80 gridded dataset from the China Meteorological Administration (CMA) as input data together with
81 other covariates, including elevation, aspect, slope, topographic wetness index (TWI), latitude, and
82 longitude. The dataset was created in three steps: (1) preparation of input data and covariates; (2)
83 the creation of the gridded dataset using comprehensive statistical analyses; and (3) an evaluation
84 of the accuracy of the gridded dataset and accuracy comparison with other three existing products
85 that use meteorological station data.

86 **2 Data**

87 **2.1 The CMA dataset and meteorological stations data**

88 The CMA dataset, which includes the daily surface temperature $0.5^\circ \times 0.5^\circ$ gridded dataset and
89 the daily precipitation $0.5^\circ \times 0.5^\circ$ gridded dataset for China (V2.0) (<https://data.cma.cn/>, last access:
90 15 September, 2022), was obtained from the China Meteorological Data Service Centre and was
91 used as the basic input data. The researchers also reported daily precipitation $0.5^\circ \times 0.5^\circ$ gridded
92 dataset during 1961-2010 from CAM dataset (Zhao and Zhu, 2015). The daily dataset of surface
93 climatological data for China (V3.0) (<https://data.cma.cn/>, last access: 15 September, 2022), which
94 includes 699 meteorological stations, was also obtained from the China Meteorological Data Service
95 Centre and was used to evaluate the new dataset (Fig. 1).

96 **2.2 Topographic data**

97 The basic topographic data, including elevation, flow direction, and flow accumulation with a
98 30 second (approximately 1 km) resolution, were obtained from the HydroSHEDS database. More
99 detailed information can be found at these links: <http://www.worldwildlife.org/hydrosheds> (last
100 access: 15 September, 2022) for general information and <http://hydrosheds.cr.usgs.gov> (last
101 access: 15 September, 2022) for data download and technical information. The “Aspect” and
102 “Slope” option of the Spatial Analyst Tools in ArcGIS10.6 were used to calculate aspect and slope.
103 The specific catchment area (SCA) was calculated based on flow direction and flow accumulation.
104 The TWI is formulated as follow:

$$105 \quad \text{TWI} = \ln\left(\frac{\text{SCA}}{\tan(\text{Slope})}\right) \quad (1)$$

105 where TWI and SCA is topographic wetness index and specific catchment area, respectively.

106 **2.3 Other datasets**

107 We used observed data from meteorological stations (Fig. 1) to evaluate our dataset and the
108 existing three daily datasets, then the accuracy of the existing three daily datasets was compared to
109 that of our dataset, respectively. The China Meteorological Administration Land Data
110 Assimilation System (CLDAS) version 2 dataset was provided by the China Meteorological Data
111 Service Centre (<https://data.cma.cn/>, last access: 15 September, 2022) for 2017 to 2019 with a
112 0.0625° (approximately 7.5 km) spatial resolution and a 1 day temporal resolution. The China
113 Meteorological Forcing Dataset (CMFD) (He et al., 2020; Yang and He, 2019) was obtained from
114 the National Tibetan Plateau Third Pole Environment Data Center (<https://data.tpdc.ac.cn/>, last
115 access: 15 September, 2022) for 1979 to 2018 with a spatial resolution of 0.1° (approximately 12
116 km) and a temporal resolution of 1 day. The historical dataset relating to the Inter-Sectoral Impact
117 Model Intercomparison Project (ISIMIP3a) was obtained from the web (<https://data.isimip.org/>,
118 last access: 15 September, 2022) for 1961 to 2016 with a spatial resolution of 0.5° (approximately
119 60 km) and a temporal resolution of 1 day. The daily maximum temperature, minimum
120 temperature, and precipitation data in the CLDAS and ISIMIP3a were used for evaluation and
121 comparison. The daily average temperature and precipitation data from the CMFD was also used
122 for evaluation and comparison.

123 **3 Methods**

124 **3.1 The input data and covariates**

125 In this study, the input data (dependent variable) was the daily $0.5^\circ \times 0.5^\circ$ CMA dataset, which
126 includes daily maximum temperature, minimum temperature and precipitation. Other covariates

127 (independent variables) included elevation, aspect, slope, TWI (with a spatial resolution of 1 km),
128 latitude, and longitude.

129 **3.2 The interpolation scheme**

130 As shown in Figure 2, the different combinations of six algorithms, which are the boosted
131 regression trees (BRT), random forests (RF), neural networks (NN), multivariate adaptive
132 regression splines (MAR), support vector machines (SVM) and the generalized additive model
133 (GAM), to predict the input data. Firstly, through k-fold cross validation ($k = 10$), the input data was
134 randomly divided into 10 sub-training datasets and sub-testing datasets. Each algorithm runs in a
135 loop through all the sub-training sets and calculates the residuals from the sub-testing sets. The
136 residuals obtained in each loop are retained. The residual of each algorithm is assigned a weight of
137 0-1 and summed up, and the ensemble of models that has the lowest residual sum is chosen. After
138 determining the best ensemble of models, surface results were interpolated using the best ensemble
139 of models, input data and covariates. The thin-plate-smoothing splines (TPS) is used to correct
140 residual error from the ensemble of models. Therefore, residuals of the ensemble are calculated from
141 the input data and these values are interpolated using TPS. Surface results from the ensemble add
142 residuals from the thin-plate-smoothing splines to get the surface result of final model. Compare R^2
143 of surface result from the ensemble and final model, and retain the surface result with higher R^2 .

144 **3.3 The interpolation methods**

145 The introduction of individual algorithm (method) and the implementations for model training
146 (R packages and functions) of that is as follows. After the model training, the function 'predict' in
147 R package 'raster' used to implemented spatial interpolation for BRT, RF, NN, MAR, SVM and

148 GAM model, and the function ‘interpolate’ in R package ‘raster’ used to spatial interpolation for
149 TPS. More details on R packages and functions could refer the web
150 (<https://www.rdocumentation.org/>, last access: 15 September, 2022).

151 **3.3.1 The BRT model**

152 As a powerful tool for exploratory regression analysis, BRT is a combination of two techniques:
153 decision trees and boosting method (Elith et al., 2008). The BRT can automatically detect the best
154 fit and is robust to missing values and outliers, therefore, BRT now widely used in remote sensing,
155 species distribution and meteorological interpolation (Pouteau et al., 2011; Appelhans et al., 2015;
156 Froeschke and Froeschke, 2011). There are two important parameters in BRT, (1) the tree
157 complexity (TC): this controls the number of splits in each tree. (2) learning rate (LR): this
158 determines the contribution of each tree to the growth model. The smaller value of LR, the more
159 trees will be built. These two parameters together determine the number of trees required for the
160 best prediction in order to find the combination of parameters that leads to the least prediction error.
161 The function ‘gbm.step’ in R package ‘dismo’ for the BRT implementation. The tree complexity
162 was set at 5, the learning rate was set at 0.001. In addition, the ‘bag.fraction’, which specifies the
163 proportion of data to be selected at each step, was set at 0.5 and other parameters are default values
164 in ‘gbm.step’.

165 **3.3.2 The RF model**

166 Like BRT, the main technology of RF also includes decision trees, however, the way in which
167 the data to build the trees is selected is different (boosting method for BRT, bagging method for RF).
168 For regression analysis, the bagging method, which take a random subset of all data for each new
169 tree that is built, makes the final output based on average of multiple trees (Breiman, 2001). As one

170 of the most accurate algorithms, RF has been used widely for predicting spatio-temporal variables,
171 such as temperature and precipitation (He et al., 2016; Mital et al., 2020; Webb et al., 2016). The
172 function ‘randomForest’ in R package ‘randomForest’ for the RF implementation. The importance
173 was set TRUE, and other parameters are default values in ‘randomForest’.

174 **3.3.3 The NN model**

175 As a powerful set of tools for solving problems in pattern recognition, data processing, and
176 non-linear control (Bishop, 1994), the NN consists of a large number of nodes and connections and
177 it includes input layer, hidden layer and output layer (Lek and Guégan, 1999). Information from
178 each node in the input layer is fed to the hidden layer. Connections between input layer nodes and
179 hidden layer nodes can all be given specific weights according to their importance. The connection
180 between the hidden layer and the output layer is also weighted, so the output is the result of the
181 weighted sum of the hidden nodes. Information transfer between hidden layer and output layer
182 through transfer function. Since the 1980s, the NN has been used in a number of fields, such as
183 prediction for meteorological variables (Snell et al., 2000; Lek and Guégan, 1999; Tang et al., 2020).
184 The function ‘nnet’ in R package ‘nnet’ for the NN implementation. The number of units in the
185 hidden layer (size) was set 10, the transfer function is linear for the output layer (linout was set
186 TRUE), the maximum number of iterations (maxit) was set 10000, and other parameters are default
187 values in ‘nnet’.

188 **3.3.4 The MAR model**

189 The MAR is an extension of linear model, which can build multiple linear regression models
190 within the range of predictive variable values by partitioning data (Friedman, 1991; Friedman and
191 Roosen, 1995). The MAR consists of two steps: firstly, it creates a set of so-called basis functions.

192 In this process, the range of predictive variable values is divided into several groups. For each group,
193 separate linear regression was modeled. Secondly, MAR estimates a least square model with its
194 basis function as the independent variable. Overfitting is avoided by iterating to remove the basis
195 functions that contribute least to the model fitting. The MAR works well with a large number of
196 predictor variables, automatically detects interactions between variables and is robust to outliers,
197 therefore, studies has done on downscaling or predicting meteorological data using MAR (Panda et
198 al., 2022; Li et al., 2019a; Zawadzka et al., 2020). The function ‘earth’ in R package ‘earth’ for the
199 MAR implementation. Use linear model to estimate standard deviation as a function of the predicted
200 response (varmod.method = ‘lm’). The nfold was set 10, the ncross was set 30, and other parameters
201 are default values in ‘earth’.

202 **3.3.5 The SVM model**

203 The SVM is also one of the machine learning supervised algorithms and mainly deals with the
204 ideas of classification and regression (Vapnik, 1999; Vapnik, 1991; Brereton and Lloyd, 2010). The
205 SVM is well supported by mathematical theory and can use kernel tricks to efficiently process non-
206 linear data. With the development of SVM, it also has been widely used in the regression and
207 prediction of meteorological variables (Belaid and Mellit, 2016; Chen et al., 2010; Tripathi et al.,
208 2006). In this study, the function ‘ksvm’ in R package ‘kernlab’ for the SVM implementation and
209 all parameters are default values in ‘ksvm’.

210 **3.3.6 The GAM model**

211 The GAM is an extension of the generalized linear model (GLM). Like GLM, GAM consists
212 of three important components: the probability distribution of the dependent variable, the linear
213 predictor and the link function, however, in GAM, the coefficient of the independent variable in the

214 linear is replaced by a sum of smooth functions (Hastie and Tibshirani, 2017; Liu, 2008). Because
215 the GAM can deal with nonlinear and non-monotone relationships between dependent and
216 independent variables, it has been used to predict and interpolate meteorological data (Hjort et al.,
217 2016; Burnett and Anderson, 2019; Aalto et al., 2013). The function ‘gam’ in R package ‘mgcv’ for
218 the GAM implementation and all parameters are default values in ‘gam’.

219 **3.3.7 The TPS method**

220 As a traditional interpolation method, the TPS has been widely used to spatially interpolate
221 surface climate data (Gong et al., 2022; Hancock and Hutchinson, 2006; Risk and James, 2022). In
222 this study, it used to correct residual error from the ensemble of models. The function ‘Tps’ in R
223 package ‘fields’ for the TPS implementation. The matrix of independent variables consists latitude
224 and longitude, the vector of dependent variables is residual error in the combinations of above
225 algorithms, and other parameters are default values in ‘Tps’.

226 **3.4 The interpolation implementation**

227 A complete operation was constructed per day per variable, so there were 64647 operations
228 (21549 days \times 3 variables) from January 1, 1961 to December 31, 2019 for maximum temperature,
229 minimum temperature and precipitation. A complete operation for a day per variable requires a
230 Central Processing Unit core, 18 G of operating memory, and 2 hours of time. In order to shorten
231 the running time, we carried out parallel computing on a supercomputer platform. Spatial
232 interpolation work was executed by R version 4.0.2 (R Core Team, 2018) and the R package
233 "machisplin" (Brown, 2019) was referenced to achieve it.

234 3.5 Evaluation metrics

235 The mean absolute error (MAE), root mean square error (RMSE), Pearson's correlation
236 coefficient (Cor), coefficient of determination after adjustment (R^2), and Nash-Sutcliffe modeling
237 efficiency (NSE) were used to evaluate the interpolation results. Pearson's correlation coefficient
238 was used to evaluate the correlation between the simulated and observed values and the other
239 metrics are defined separately as follows:

$$MAE = \frac{1}{n} \sum_{i=1}^n |S_i - O_i| \quad (2)$$

$$RMSE = \sqrt{\frac{1}{n} \sum_{i=1}^n (S_i - O_i)^2} \quad (3)$$

$$R^2 = 1 - \left(1 - \frac{\sum_{i=1}^n (S_i - \bar{O})^2}{\sum_{i=1}^n (O_i - \bar{O})^2}\right) \frac{(n-1)}{(n-k-1)} \quad (4)$$

$$NSE = 1 - \frac{\sum_{i=1}^n (S_i - O_i)^2}{\sum_{i=1}^n (O_i - \bar{O})^2} \quad (5)$$

240 where S_i and O_i are the model predicted and the experimentally observed values, respectively;
241 \bar{O} is the mean of the observed values; n is the number of observations; and k is the value of the
242 independent variable. High Cor, R^2 , and NSE values, and small RMSE and MAE values indicate
243 the strength of agreement between the predicted and observed values.

244 4 Results and discussion

245 4.1 Validation of temperature and precipitation

246 The spatial interpolation results, including daily maximum temperature, minimum temperature,
247 and precipitation, were validated using meteorological station data. The results of the validation

248 showed that the daily maximum and minimum temperatures were highly accurate (Fig. 3 and Table
249 1). The fitting slopes between the simulated and observed values were both close to 1 and the
250 coefficients of determination after adjustment were 0.98 and 0.99, respectively, for daily maximum
251 and minimum temperature (Figs. 3a, b). As shown in Table 1, the MAE was 1.07 °C and 1.08 °C,
252 and the RMSE was 1.62 °C and 1.53 °C for daily maximum and minimum temperatures, respectively.
253 In addition, the Cor and NSE values were close to 1 for both the daily maximum and minimum
254 temperatures. Daily precipitation was less accurate than temperature with an R^2 of 0.71 (Fig. 3c),
255 which was mainly caused by underestimating high daily precipitation. However, most of the points
256 were concentrated in the low daily precipitation section. Furthermore, the MAE and RMSE for daily
257 precipitation were 1.30 mm and 4.78 mm, respectively; the Cor between the simulated and observed
258 daily precipitation was 0.84, and the NSE was 0.70 (Table 1).

259 The interpolation accuracy shows spatial differences (Fig. 4). The R^2 values of the daily
260 maximum and minimum temperatures in southwest China were less than 0.94 and lower than those
261 for other regions (Figs. 4a, c). The mean absolute errors for the daily maximum and minimum
262 temperature ranges at most meteorological stations were less than 1 °C. However, there were some
263 meteorological stations with mean absolute errors of more than 2 °C and these were evenly
264 distributed across China (Figs. 4b, d). The R^2 value for daily precipitation at most meteorological
265 stations was greater than 0.7 and the MAE decreased from south to north across China (Figs. 4e, f).
266 For precipitation where the R^2 map (Fig. 4e) shows a west-east gradient in the scores that is
267 different from the north-south gradient in the MAE map (Fig. 4f). There are fewer meteorological
268 observation stations in the western region than in the eastern region, which may lead to the subtle

269 east-west gradient of the R^2 value for daily precipitation. The obvious north-south gradient for
270 MAE of daily precipitation could be caused by the rainfall frequency (Fig. 4f, Fig. 5), the MAE of
271 monthly precipitation in China from other study showed a similar pattern (Peng et al., 2019).
272 Rainfall frequency above light rainfall, which is defined as a daily rainfall from 0 to 4 mm (Alpert et
273 al., 2002), is strongly correlated with the MAE of daily precipitation (illustration in Fig. 5), so that
274 the MAE of daily precipitation in the southern region with higher rainfall frequency is larger than
275 that in the northern region with lower rainfall frequency.

276 The meteorological stations were divided into the middle and lower reaches of the Yangtze
277 River (MLYR), North China (NC), Northeast China (NEC), Northwest China (NWC), South China
278 (SC), and Southwest China (SWC) (Fig. 1) according to their diverse geographic and climatic
279 conditions and administrative areas (Qin, et al., 2022). The cumulative distribution functions curve
280 trend of difference between the simulated and observed values was always similar for daily
281 maximum temperature, minimum temperature, and precipitation in the six regions, as well as in
282 whole China. The daily maximum and minimum temperatures were all underestimated in the MLYR,
283 NEC, NWC, SC, and SWC (Fig. 6a). The daily minimum temperatures were all underestimated in
284 the MLYR, NC, NWC, SC, and SWC (Fig. 6b). For both daily maximum and minimum
285 temperatures, the lowest average difference between the simulated and observed values occurred in
286 NC and NEC, while the greatest difference occurred in SWC (Figs. 6a,b). Except in the NWC region,
287 the average difference between simulated and observed values for daily precipitation was less than
288 0 mm in the other regions (Fig. 6c). The largest averages difference between simulated and observed
289 for daily precipitation occurred in the SC region, with a value of 0.49 mm (Fig. 6c). Across whole

290 China, the average difference between simulated and observed values for daily maximum
291 temperature, minimum temperature, and precipitation was 0.36 °C, 0.30 °C and 0.12 mm,
292 respectively.

293 **4.2 Temporal and spatial distributions of temperature and precipitation**

294 The results showed that detailed spatial changes in temperature and precipitation over time
295 could be obtained (Fig. 7). For example, the increase in annual average values (both maximum
296 temperature and minimum temperature) were obvious over the Tibetan Plateau from 1965 to 2010
297 (Figs. 7a–h, the d1 and h1 subregions). In addition, compared with other years, the annual average
298 daily minimum temperature clearly increased in some areas of NWC (Figs. 7e–h, the h2 and h3
299 subregions) and MLYR (Figs. 7e–h, the h4 subregion) in 2010. The most significant annual
300 precipitation changes occurred in NEC (Figs. 7i–l, the l1 subregion) between 1965 and 2010.

301 The distributions of annual average daily maximum and minimum temperatures and annual
302 precipitation across the six regions of China in 1965, 1980, 1995, and 2010 were analyzed (Fig. 8).
303 Compared with other years, the areas with smaller values for annual average daily maximum
304 temperature (less than 0) and annual average daily minimum temperature (less than –10) in SWC
305 and NWC decreased in 2010 (Figs. 8a1, 8a2, 8b1, 8b2). These areas are mainly distributed on the
306 Qinghai-Tibet Plateau, which has seen a large increase in temperature over the past few decades.
307 The density distribution peak for the annual average daily maximum and minimum temperatures in
308 NEC moved to the right from 1965 to 1995, but moved to the left in 2010 (Figs. 8a3, 8b3). The
309 mean annual average daily minimum temperature in 2010 was higher in the MLYR, NC, and SC
310 than in the other three years (Figs. 8b4–6). There was an increase in mean annual precipitation in

311 the northern part of China over the period 1965–2010 (Figs. 8c2–4). It increased from 335 mm to
312 415 mm across NWC (Fig. 8c2), from 487 mm to 593 mm across NEC (Fig. 8c3), and from 531
313 mm to 654 mm across NC (Fig. 8c4). In the MLYR, there were more areas with annual precipitation
314 of less than 1000 mm, and areas with an annual precipitation of more than 2000 mm increased in
315 1995 and 2010 compared 1965 and 1980 (Fig. 8c5). Similarly, compared with other years, there
316 were more areas with annual precipitation of less than 1000 mm and more than 2000 mm in SC in
317 2010 (Fig. 8c6).

318 **4.3 Accuracy comparison with other products**

319 The performances of the CMFD, CLDAS and ISIMIP3a generated daily temperatures and
320 precipitations were evaluated against observations from all the meteorological stations and
321 compared their performance with that of our dataset (Figs. 9–11; Tables 2–4). The fitting slopes
322 between the simulated and observed daily temperature values were always close to 1 for all datasets
323 (Figs. 9a–c; Figs. 10a–d; Figs. 11a–d). The R^2 for the CMFD daily average temperature was
324 slightly smaller than that for daily minimum temperature in our dataset (Figs. 9b, c), but was equal
325 to our data set for daily maximum temperature (Figs. 9a, c). The Cor and NSE for the CMFD daily
326 average temperature were also similar to our estimated daily maximum and minimum temperatures
327 (Table 2). By contrast, the MAE and RMSE for the CMFD daily average temperature were 1.12 °C
328 and 1.64 °C, respectively, which were greater than for our estimated daily maximum and minimum
329 temperatures (Table 2). The MAEs of daily maximum and minimum temperature for our dataset
330 were 1.07 °C and 1.08 °C respectively; and the RMSEs of daily maximum and minimum
331 temperature for our dataset were 1.63 °C and 1.54 °C, respectively, between 1979 and 2018 (Table

332 2). The R^2 , Cor, NSE, MAE, and RMSE for the CLDAS daily maximum temperatures were 0.91,
333 0.95, 0.90, 2.54 °C, and 3.63 °C, respectively. Accuracy clearly improved for our daily maximum
334 temperature, and the corresponding metrics were 0.98, 0.99, 0.98, 1.10 °C, and 1.73 °C (Figs. 10a,
335 b; Table 3). The MAE and RMSE for the CLDAS daily minimum temperature were clearly higher
336 than our estimates for daily minimum temperature, and the R^2 , Cor, and NSE for daily minimum
337 temperature in our dataset were higher than those for the CLDAS daily minimum temperature (Figs.
338 10c, d; Table 3), thus indicating that the accuracy of our daily minimum temperature estimates was
339 superior to that of the CLDAS daily minimum temperature product. Compared with the ISIMIP3a,
340 the R^2 , Cor, and NSE of daily maximum and minimum temperature in our dataset are always higher
341 and the MAE and RMSE of these are always smaller (Figs. 11 a–d; Table 4).

342 The R^2 value for our estimated daily precipitation clearly improved compared to the other
343 three datasets, especially the ISIMIP3a and CLDAS dataset (Figs. 9d, e; Figs. 10e, f; Figs. 11e, f).
344 The Cor and NSE for the CMFD daily precipitation were obviously smaller than those for our
345 dataset, and the RMSE for CMFD daily precipitation were greater than those for our dataset (Table
346 2). During 2017–2019, the Cor, NSE, MAE, and RMSE for our estimated daily precipitation were
347 0.84, 0.70, 1.42 mm, and 4.93 mm, respectively, and the corresponding values for the CLDAS daily
348 precipitation changed to 0.58, 0.28, 2.36 mm, and 7.67 mm, respectively (Table 3). During 1961–
349 2016, the Cor, NSE, MAE, and RMSE for our estimated daily precipitation were 0.84, 0.70, 1.30
350 mm, and 4.78 mm, respectively, and the corresponding values for the ISIMIP3a daily precipitation
351 changed to 0.48, 0.14, 2.75 mm, and 8.10 mm, respectively (Table 4). Thus, the daily precipitation
352 accuracy of our dataset was generally higher than that of CMFD, CLDAS and ISIMIP3a.

353 **5 Data availability**

354 The HRLT dataset includes daily maximum temperature, minimum temperature, and
355 precipitation at a 1 km spatial resolution across China from January 1961 to December 2019. The
356 datasets are publicly available in NetCDF format at <https://doi.org/10.1594/PANGAEA.941329>
357 (Qin and Zhang, 2022).

358 **6 Conclusions**

359 The result of this study is a high-resolution (1 km) daily gridded maximum temperature,
360 minimum temperature and precipitation dataset across China for the long-term (1961–2019)
361 (HRLT). The HRLT dataset shows an overall high correlation with the observations from
362 meteorological stations for daily maximum and minimum temperatures (R^2 was 0.98 and 0.99,
363 respectively; Cor were both 0.99; NSE was 0.98 and 0.99, respectively) and the errors were smaller
364 (MAE was 1.07 °C and 1.08 °C, respectively; RMSE was 1.62 °C and 1.53 °C, respectively).
365 Although the HRLT dataset showed that the daily precipitation accuracy was lower than the daily
366 temperature accuracy (R^2 , Cor, NSE, MAE, and RMSE were 0.71, 0.84, 0.70, 1.30 mm, and 4.78
367 mm, respectively), the daily precipitation data in the HRLT dataset were more accurate and had a
368 finer spatial resolution compared to the other three existing datasets (CMFD, CLDAS and
369 ISIMIP3a). Furthermore, the accuracies for daily maximum and minimum temperatures and
370 precipitation were lower in the southwestern part of China, probably because of the complex
371 topography in that area compared to other areas. Calculation and interpolation by subregions may
372 solve this problem in future studies. The use of satellite data as an input covariate in future studies
373 will further improve the accuracy of the HRLT dataset, especially for precipitation. The HRLT

374 dataset will help identify future extreme climatic events and can be also used to improve process-
375 based models for prediction, adaptation, and mitigation strategies.

376 **Author contributions**

377 Rongzhu Qin and Feng Zhang calculated the dataset, analyzed the results, and wrote the
378 manuscript; all other authors reviewed and revised the manuscript.

379 **Competing interests**

380 The authors declare that they have no conflict of interest.

381 **Acknowledgements**

382 This study was supported by the Second Tibetan Plateau Scientific Expedition and Research
383 (Grant No. 2019QZKK0305), National Natural Science Foundation of China (Grant No. 32071550),
384 and the “111” Programme (BP0719040). We thank the Supercomputing Center of Lanzhou
385 University for providing the computing requirements for this study. We are also grateful to the China
386 Meteorological Data Service Centre, National Tibetan Plateau Third Pole Environment Data Center,
387 Potsdam Institute for Climate Impact Research and the International Institute for Applied Systems
388 Analysis for contributing datasets to the study. We are also thanking Dr. Marianne Rehage from
389 PANGAEA for processing and publishing the dataset.

390 **References**

391 Aalto, J., Pirinen, P., Heikkinen, J., and Venäläinen, A.: Spatial interpolation of monthly climate data
392 for Finland: comparing the performance of kriging and generalized additive models, *Theor Appl*
393 *Climatol*, 112, 99-111, <https://doi.org/10.1007/s00704-012-0716-9>, 2013.
394 Alpert, P., T. Ben-Gai, A. Baharad, Y. Benjamini, D. Yekutieli, M. Colacino, L. Diodato et al. The
395 paradoxical increase of Mediterranean extreme daily rainfall in spite of decrease in total values,
396 *Geophysical research letters* 29(11):31-1, <https://doi.org/10.1029/2001GL013554>, 2002.

397 Appelhans, T., Mwangomo, E., Hardy, D. R., Hemp, A., and Nauss, T.: Evaluating machine learning
398 approaches for the interpolation of monthly air temperature at Mt. Kilimanjaro, Tanzania, *Spatial*
399 *Statistics*, 14, 91-113, <https://doi.org/10.1016/j.spasta.2015.05.008>, 2015.

400 Belaid, S. and Mellit, A.: Prediction of daily and mean monthly global solar radiation using support
401 vector machine in an arid climate, *Energy Conversion and Management*, 118, 105-118,
402 <https://doi.org/10.1016/j.enconman.2016.03.082>, 2016.

403 Bishop, C. M.: *Neural networks and their applications*, Review of scientific instruments, 65, 1803-
404 1832, <https://doi.org/10.1063/1.1144830>, 1994.

405 Breiman, L.: Random forests, *Machine learning*, 45, 5-32, 2001.

406 Breerton, R. G. and Lloyd, G. R.: Support Vector Machines for classification and regression, *Analyst*,
407 135, 230-267, <https://doi.org/10.1039/B918972F>, 2010.

408 Brinckmann, S., Krähenmann, S., and Bissolli, P.: High-resolution daily gridded data sets of air
409 temperature and wind speed for Europe, *Earth Syst. Sci. Data*, 8, 491-516, [https://doi.org/10.5194/essd-](https://doi.org/10.5194/essd-8-491-2016)
410 [8-491-2016](https://doi.org/10.5194/essd-8-491-2016), 2016.

411 Interpolation of noisy multi-variate data using machine learning ensembling:
412 <https://github.com/jasonleebrown/machisplin>, last
413 Burnett, J. D. and Anderson, P. D.: Using generalized additive models for interpolating microclimate in
414 dry-site ponderosa pine forests, *Agricultural and Forest Meteorology*, 279, 107668,
415 <https://doi.org/10.1016/j.agrformet.2019.107668>, 2019.

416 Chen, S.-T., Yu, P.-S., and Tang, Y.-H.: Statistical downscaling of daily precipitation using support
417 vector machines and multivariate analysis, *J Hydrol*, 385, 13-22,
418 <https://doi.org/10.1016/j.jhydrol.2010.01.021>, 2010.

419 Chen, Y., Liang, S., Ma, H., Li, B., He, T., and Wang, Q.: An all-sky 1 km daily land surface air
420 temperature product over mainland China for 2003–2019 from MODIS and ancillary data, *Earth Syst.*
421 *Sci. Data*, 13, 4241-4261, <https://doi.org/10.5194/essd-13-4241-2021>, 2021.

422 Elith, J., Leathwick, J. R., and Hastie, T.: A working guide to boosted regression trees, *J Anim Ecol*, 77,
423 802-813, <https://doi.org/10.1111/j.1365-2656.2008.01390.x>, 2008.

424 Friedman, J. H.: Multivariate adaptive regression splines, *The annals of statistics*, 19, 1-67,
425 <https://doi.org/10.1214/aos/1176347963>, 1991.

426 Friedman, J. H. and Roosen, C. B.: An introduction to multivariate adaptive regression splines, 3, 192-
427 217, <https://doi.org/10.1177/096228029500400303>, 1995.

428 Froeschke, J. T. and Froeschke, B. F.: Spatio-temporal predictive model based on environmental factors
429 for juvenile spotted seatrout in Texas estuaries using boosted regression trees, *Fisheries Research*, 111,
430 131-138, <https://doi.org/10.1016/j.fishres.2011.07.008>, 2011.

431 Gong, H., Liu, H., Xiang, X., Jiao, F., Cao, L., and Xu, X.: 1km Monthly Precipitation and
432 Temperatures Dataset for China from 1952 to 2019 based on a Brand-New and High-Quality Baseline
433 Climatology Surface, *Earth Syst. Sci. Data Discuss.*, 2022, 1-30, 10.5194/essd-2022-45, 2022.

434 Hancock, P. A. and Hutchinson, M. F.: Spatial interpolation of large climate data sets using bivariate
435 thin plate smoothing splines, *Environmental Modelling & Software*, 21, 1684-1694,
436 <https://doi.org/10.1016/j.envsoft.2005.08.005>, 2006.

437 Hartl, L., Stuefer, M., Saito, T., and Okura, Y.: History and Data Records of the Automatic Weather
438 Station on Denali Pass (5715 m), 1990–2007, *Journal of Applied Meteorology and Climatology*, 59,
439 2113-2127, <https://doi.org/10.1175/jamc-d-20-0082.1>, 2020.

440 Hastie, T. J. and Tibshirani, R. J.: Generalized additive models, Routledge 2017.

441 He, J., Yang, K., Tang, W., Lu, H., Qin, J., Chen, Y., and Li, X.: The first high-resolution
442 meteorological forcing dataset for land process studies over China, *Scientific Data*, 7, 25,
443 <https://doi.org/10.1038/s41597-020-0369-y>, 2020.

444 He, Q., Wang, M., Liu, K., Li, K., and Jiang, Z.: GPRChinaTemp1km: a high-resolution monthly air
445 temperature dataset for China (1951–2020) based on machine learning, *Earth Syst. Sci. Data Discuss.*,
446 2021, 1-29, <https://doi.org/10.5194/essd-2021-267>, 2021.

447 He, X., Chaney, N. W., Schleiss, M., and Sheffield, J.: Spatial downscaling of precipitation using
448 adaptable random forests, *Water Resources Research*, 52, 8217-8237,
449 <https://doi.org/10.1002/2016WR019034>, 2016.

450 Herrera, S., Cardoso, R. M., Soares, P. M., Espírito-Santo, F., Viterbo, P., and Gutiérrez, J. M.:
451 Iberia01: a new gridded dataset of daily precipitation and temperatures over Iberia, *Earth Syst. Sci.*
452 *Data*, 11, 1947-1956, <https://doi.org/10.5194/essd-11-1947-2019>, 2019.

453 Hjort, J., Suomi, J., and Käyhkö, J.: Extreme urban–rural temperatures in the coastal city of Turku,
454 Finland: Quantification and visualization based on a generalized additive model, *Science of the Total*
455 *Environment*, 569, 507-517, <https://doi.org/10.1016/j.scitotenv.2016.06.136>, 2016.

456 Iizumi, T., Furuya, J., Shen, Z., Kim, W., Okada, M., Fujimori, S., Hasegawa, T., and Nishimori, M.:
457 Responses of crop yield growth to global temperature and socioeconomic changes, *Sci Rep-Uk*, 7,
458 7800, <https://doi.org/10.1038/s41598-017-08214-4>, 2017.

459 Lee, M.-H., Im, E.-S., and Bae, D.-H.: Impact of the spatial variability of daily precipitation on
460 hydrological projections: A comparison of GCM- and RCM-driven cases in the Han River basin,
461 Korea, *Hydrological Processes*, 33, 2240-2257, <https://doi.org/10.1002/hyp.13469>, 2019.

462 Lek, S. and Guégan, J. F.: Artificial neural networks as a tool in ecological modelling, an introduction,
463 *Ecol Model*, 120, 65-73, [https://doi.org/10.1016/S0304-3800\(99\)00092-7](https://doi.org/10.1016/S0304-3800(99)00092-7), 1999.

464 Lesk, C., Rowhani, P., and Ramankutty, N.: Influence of extreme weather disasters on global crop
465 production, *Nature*, 529, 84-87, <https://doi.org/10.1038/nature16467>, 2016.

466 Li, D. H. W., Chen, W., Li, S., and Lou, S.: Estimation of hourly global solar radiation using
467 Multivariate Adaptive Regression Spline (MARS) – A case study of Hong Kong, *Energy*, 186, 115857,
468 <https://doi.org/10.1016/j.energy.2019.115857>, 2019a.

469 Li, T., Zheng, X., Dai, Y., Yang, C., Chen, Z., Zhang, S., Wu, G., Wang, Z., Huang, C., Shen, Y., and
470 Liao, R.: Mapping near-surface air temperature, pressure, relative humidity and wind speed over
471 Mainland China with high spatiotemporal resolution, *Advances in Atmospheric Sciences*, 31, 1127-
472 1135, <https://doi.org/10.1007/s00376-014-3190-8>, 2014.

473 Li, Y., Guan, K., Schnitkey, G. D., DeLucia, E., and Peng, B.: Excessive rainfall leads to maize yield
474 loss of a comparable magnitude to extreme drought in the United States, *Global Change Biology*, 25,
475 2325-2337, <https://doi.org/10.1111/gcb.14628>, 2019b.

476 Liu, H.: Generalized additive model, Department of Mathematics and Statistics University of
477 Minnesota Duluth: Duluth, MN, USA, 55812, 2008.

478 Lobell, D. B., Schlenker, W., and Costa-Roberts, J.: Climate Trends and Global Crop Production Since
479 1980, *Science*, 333, 616-620, <https://doi.org/doi:10.1126/science.1204531>, 2011.

480 Lu, Y., Hu, H., Li, C., and Tian, F.: Increasing compound events of extreme hot and dry days during
481 growing seasons of wheat and maize in China, *Scientific Reports*, 8, 16700,
482 <https://doi.org/10.1038/s41598-018-34215-y>, 2018.

483 Merino, A., Guerrero-Higueras, A. M., López, L., Gascón, E., Sánchez, J. L., Lorente, J. M., Marcos, J.
484 L., Matía, P., Ortiz de Galisteo, J. P., Nafría, D., Fernández-González, S., Weigand, R., Hermida, L.,
485 and García-Ortega, E.: Development of tools for evaluating rainfall estimation models in real- time
486 using the Integrated Meteorological Observation Network in Castilla y León (Spain), 2014.

487 Mital, U., Dwivedi, D., Brown, J. B., Faybishenko, B., Painter, S. L., and Steefel, C. I.: Sequential
488 Imputation of Missing Spatio-Temporal Precipitation Data Using Random Forests, *Frontiers in Water*,
489 2, <https://doi.org/10.3389/frwa.2020.00020>, 2020.

490 Myhre, G., Alterskjær, K., Stjern, C. W., Hodnebrog, Ø., Marelle, L., Samset, B. H., Sillmann, J.,
491 Schaller, N., Fischer, E., Schulz, M., and Stohl, A.: Frequency of extreme precipitation increases
492 extensively with event rareness under global warming, *Scientific Reports*, 9, 16063,
493 <https://doi.org/10.1038/s41598-019-52277-4>, 2019.

494 Panda, K. C., Singh, R. M., Thakural, L. N., and Sahoo, D. P.: Representative grid location-multivariate
495 adaptive regression spline (RGL-MARS) algorithm for downscaling dry and wet season rainfall, *J*
496 *Hydrol*, 605, 127381, <https://doi.org/10.1016/j.jhydrol.2021.127381>, 2022.

497 Peng, S., Y. Ding, W. Liu, and Z. Li. 1 km monthly temperature and precipitation dataset for
498 China from 1901 to 2017. *Earth Syst. Sci. Data* 11:1931-1946, [https://doi.org/10.5194/essd-11-1931-](https://doi.org/10.5194/essd-11-1931-2019)
499 [2019](https://doi.org/10.5194/essd-11-1931-2019), 2019.

500 Pouteau, R., Rambal, S., Ratte, J.-P., Gogé, F., Joffre, R., and Winkel, T.: Downscaling MODIS-derived
501 maps using GIS and boosted regression trees: The case of frost occurrence over the arid Andean
502 highlands of Bolivia, *Remote Sens Environ*, 115, 117-129, <https://doi.org/10.1016/j.rse.2010.08.011>,
503 2011.

504 Qin, R. and Zhang, F.: HRLT: A high-resolution (1 day, 1 km) and long-term (1961–2019) gridded
505 dataset for temperature and precipitation across China, PANGAEA [dataset],
506 <https://doi.org/10.1594/PANGAEA.941329>, 2022.

507 Qin, R., F. Zhang, C. Yu, Q. Zhang, J. Qi, and F.-m. Li: Contributions made by rain-fed potato with
508 mulching to food security in China, *European Journal of Agronomy*, 133, 126435,
509 <https://doi.org/10.1016/j.eja.2021.126435>, 2022.

510 R Core Team: R: A Language and Environment for Statistical Computing (3.5) [code], 2018.

511 Rao, B. B., Chowdary, P. S., Sandeep, V. M., Pramod, V. P., and Rao, V. U. M.: Spatial analysis of the
512 sensitivity of wheat yields to temperature in India, *Agr Forest Meteorol*, 200, 192-202,
513 <https://doi.org/10.1016/j.agrformet.2014.09.023>, 2015.

514 Risk, C. and James, P. M. A.: Optimal Cross-Validation Strategies for Selection of Spatial Interpolation
515 Models for the Canadian Forest Fire Weather Index System, *Earth and Space Science*, 9,
516 e2021EA002019, <https://doi.org/10.1029/2021EA002019>, 2022.

517 Sadeghi, M., Nguyen, P., Naeini, M. R., Hsu, K., Braithwaite, D., and Sorooshian, S.: PERSIANN-
518 CCS-CDR, a 3-hourly 0.04° global precipitation climate data record for heavy precipitation studies, *Sci*
519 *Data*, 8, 157, <https://doi.org/10.1038/s41597-021-00940-9>, 2021.

520 Schamm, K., Ziese, M., Becker, A., Finger, P., Meyer-Christoffer, A., Schneider, U., Schröder, M., and
521 Stender, P.: Global gridded precipitation over land: a description of the new GPCP First Guess Daily
522 product, *Earth Syst. Sci. Data*, 6, 49-60, <https://doi.org/10.5194/essd-6-49-2014>, 2014.

523 Sekulić, A., Kilibarda, M., Protić, D., and Bajat, B.: A high-resolution daily gridded meteorological
524 dataset for Serbia made by Random Forest Spatial Interpolation, *Sci Data*, 8, 123,
525 <https://doi.org/10.1038/s41597-021-00901-2>, 2021.

526 Shi, C., Xie, Z., Qian, H., Liang, M., and Yang, X.: China land soil moisture EnKF data assimilation
527 based on satellite remote sensing data, *Science China Earth Sciences*, 54, 1430-1440,
528 <https://doi.org/10.1007/s11430-010-4160-3>, 2011.

529 Snell, S. E., Gopal, S., and Kaufmann, R. K.: Spatial interpolation of surface air temperatures using
530 artificial neural networks: Evaluating their use for downscaling GCMs, *Journal of Climate*, 13, 886-
531 895, [https://doi.org/10.1175/1520-0442\(2000\)013<0886:SIOSAT>2.0.CO;2](https://doi.org/10.1175/1520-0442(2000)013<0886:SIOSAT>2.0.CO;2), 2000.

532 Tang, G., Clark, M. P., Newman, A. J., Wood, A. W., Papalexiou, S. M., Vionnet, V., and Whitfield, P.
533 H.: SCDNA: a serially complete precipitation and temperature dataset for North America from 1979 to
534 2018, *Earth Syst. Sci. Data*, 12, 2381-2409, <https://doi.org/10.5194/essd-12-2381-2020>, 2020.

535 Tripathi, S., Srinivas, V. V., and Nanjundiah, R. S.: Downscaling of precipitation for climate change
536 scenarios: A support vector machine approach, *J Hydrol*, 330, 621-640,
537 <https://doi.org/10.1016/j.jhydrol.2006.04.030>, 2006.

538 Vapnik, V.: Principles of risk minimization for learning theory, *Advances in neural information*
539 *processing systems*, 4, 1991.

540 Vapnik, V. N.: An overview of statistical learning theory, *IEEE transactions on neural networks*, 10,
541 988-999, <https://doi.org/10.1109/72.788640>, 1999.

542 Wang, B., Liu, L., O'Leary, G. J., Asseng, S., Macadam, I., Lines-Kelly, R., Yang, X., Clark, A., Crean,
543 J., Sides, T., Xing, H., Mi, C., and Yu, Q.: Australian wheat production expected to decrease by the late
544 21st century, *Global Change Biol*, 24, 2403-2415, <https://doi.org/10.1111/gcb.14034>, 2018.

545 Webb, M. A., Hall, A., Kidd, D., and Minansy, B.: Local-scale spatial modelling for interpolating
546 climatic temperature variables to predict agricultural plant suitability, *Theor Appl Climatol*, 124, 1145-
547 1165, <https://doi.org/10.1007/s00704-015-1461-7>, 2016.

548 Xu, C., McDowell, N. G., Fisher, R. A., Wei, L., Sevanto, S., Christoffersen, B. O., Weng, E., and
549 Middleton, R. S.: Increasing impacts of extreme droughts on vegetation productivity under climate
550 change, *Nature Climate Change*, 9, 948-953, <https://doi.org/10.1038/s41558-019-0630-6>, 2019.

551 Yang, E.-G., Kim, H. M., Kim, J., and Kay, J. K.: Effect of Observation Network Design on
552 Meteorological Forecasts of Asian Dust Events, *Monthly Weather Review*, 142, 4679-4695,
553 <https://doi.org/10.1175/mwr-d-14-00080.1>, 2014.

554 Yang, K. and He, J.: China meteorological forcing dataset (1979-2018) [dataset],
555 <https://doi.org/10.11888/AtmosphericPhysics.tpe.249369.file.>, 2019.

556 Zawadzka, J., Corstanje, R., Harris, J., and Truckell, I.: Downscaling Landsat-8 land surface
557 temperature maps in diverse urban landscapes using multivariate adaptive regression splines and very
558 high resolution auxiliary data, *International Journal of Digital Earth*, 13, 899-914,
559 <https://doi.org/10.1080/17538947.2019.1593527>, 2020.

560 Zhang, F., Zhang, W., Qi, J., and Li, F.-M.: A regional evaluation of plastic film mulching for
561 improving crop yields on the Loess Plateau of China, *Agr Forest Meteorol*, 248, 458-468,
562 <https://doi.org/10.1016/j.agrformet.2017.10.030>, 2018.

563 Zhao, Y. and Zhu, J.: Accuracy and evaluation of precipitation grid daily data sets in China in recent 50
564 years (in Chinese), *Plateau Meteorology*, 34, 50-58, <https://doi.org/10.7522/j.issn.1000-0534.2013.00141>, 2015.

566

Table 1 Summary of the accuracies for the HRLT datasets using data from the meteorological stations

Variable	MAE	RMSE	Cor	NSE	N	Period
Maximum temperature (°C)	1.07	1.62	0.99	0.98	14731830	1961–2019
Minimum temperature (°C)	1.08	1.53	0.99	0.99	14730410	1961–2019
Precipitation (mm)	1.30	4.78	0.84	0.70	14730380	1961–2019

MAE, RMSE, Cor, and NSE are the mean absolute error, root mean square error, Pearson's correlation coefficient, and Nash-Sutcliffe modeling efficiency, respectively. N is the number of observations and Period is the beginning to end years of the data.

Table 2 Comparison of accuracies for the HRLT and CMFD datasets using data from the meteorological stations

Variable	Dataset	MAE	RMSE	Cor	NSE	N	Period
Maximum temperature (°C)	HRLT	1.07	1.63	0.99	0.98	9969602	1979–2018
Minimum temperature (°C)	HRLT	1.08	1.54	0.99	0.99	9969602	1979–2018
Average temperature (°C)	CMFD	1.12	1.64	0.99	0.98	9969602	1979–2018
Precipitation (mm)	HRLT	1.30	4.73	0.84	0.71	9968784	1979–2018
	CMFD	1.30	5.85	0.75	0.55	9968784	1979–2018

MAE, RMSE, Cor, and NSE are the mean absolute error, root mean square error, Pearson’s correlation coefficient, and Nash-Sutcliffe modeling efficiency, respectively. N is the number of observations and Period is the beginning to end years of the data.

Table 3 Comparison of accuracies for the HRLT and the CLDAS datasets using data from the meteorological stations

Variable	Dataset	MAE	RMSE	Cor	NSE	N	Period
Maximum temperature (°C)	HRLT	1.10	1.73	0.99	0.98	686653	2017–2019
	CLDAS	2.54	3.63	0.95	0.90	686653	2017–2019
Minimum temperature (°C)	HRLT	1.14	1.65	0.99	0.98	686653	2017–2019
	CLDAS	1.58	2.63	0.98	0.95	686653	2017–2019
Precipitation (mm)	HRLT	1.42	4.93	0.84	0.70	685936	2017–2019
	CLDAS	2.36	7.67	0.58	0.28	685936	2017–2019

MAE, RMSE, Cor, and NSE are the mean absolute error, root mean square error, Pearson’s correlation coefficient, and Nash-Sutcliffe modeling efficiency, respectively. N is the number of observations and Period is the beginning to end years of the data.

Table 4 Comparison of accuracies for the HRLT and the ISIMP3a datasets using data from the meteorological stations

Variable	Dataset	MAE	RMSE	Cor	NSE	N	Period
Maximum temperature (°C)	HRLT	1.06	1.61	0.99	0.98	13973110	1961–2016
	ISIMP3a	2.47	3.47	0.96	0.91	13973110	1961–2016
Minimum temperature (°C)	HRLT	1.07	1.52	0.99	0.99	13971690	1961–2016
	ISIMP3a	2.63	3.60	0.96	0.92	13971690	1961–2016
Precipitation (mm)	HRLT	1.30	4.78	0.84	0.70	13971680	1961–2016
	ISIMP3a	2.75	8.10	0.48	0.14	13971680	1961–2016

MAE, RMSE, Cor, and NSE are the mean absolute error, root mean square error, Pearson’s correlation coefficient, and Nash-Sutcliffe modeling efficiency, respectively. N is the number of observations and Period is the beginning to end years of the data.

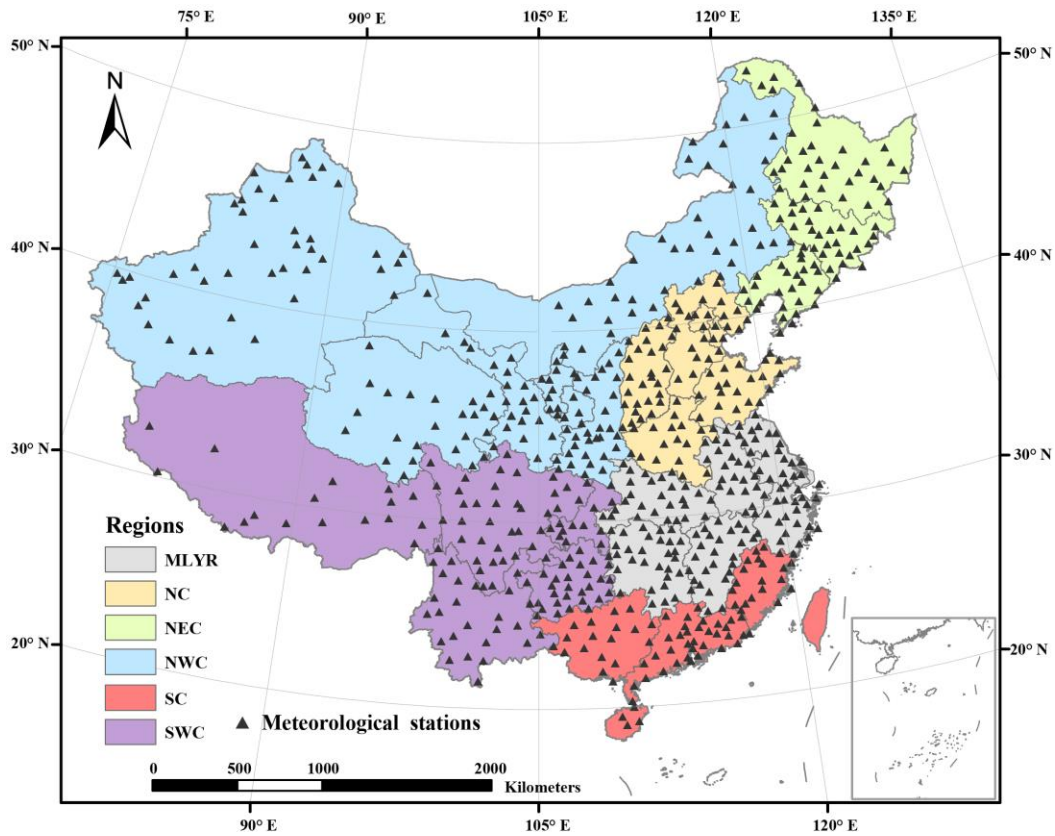


Figure 1. Regions and spatial distribution of the meteorological stations in China. MLYR, NC, NEC, NWC, SC, and SWC are the Middle and Lower reaches of the Yangtze River, North China, Northeast China, Northwest China, South China, and Southwest China, respectively. Note: meteorological stations data were missing for Taiwan Province.

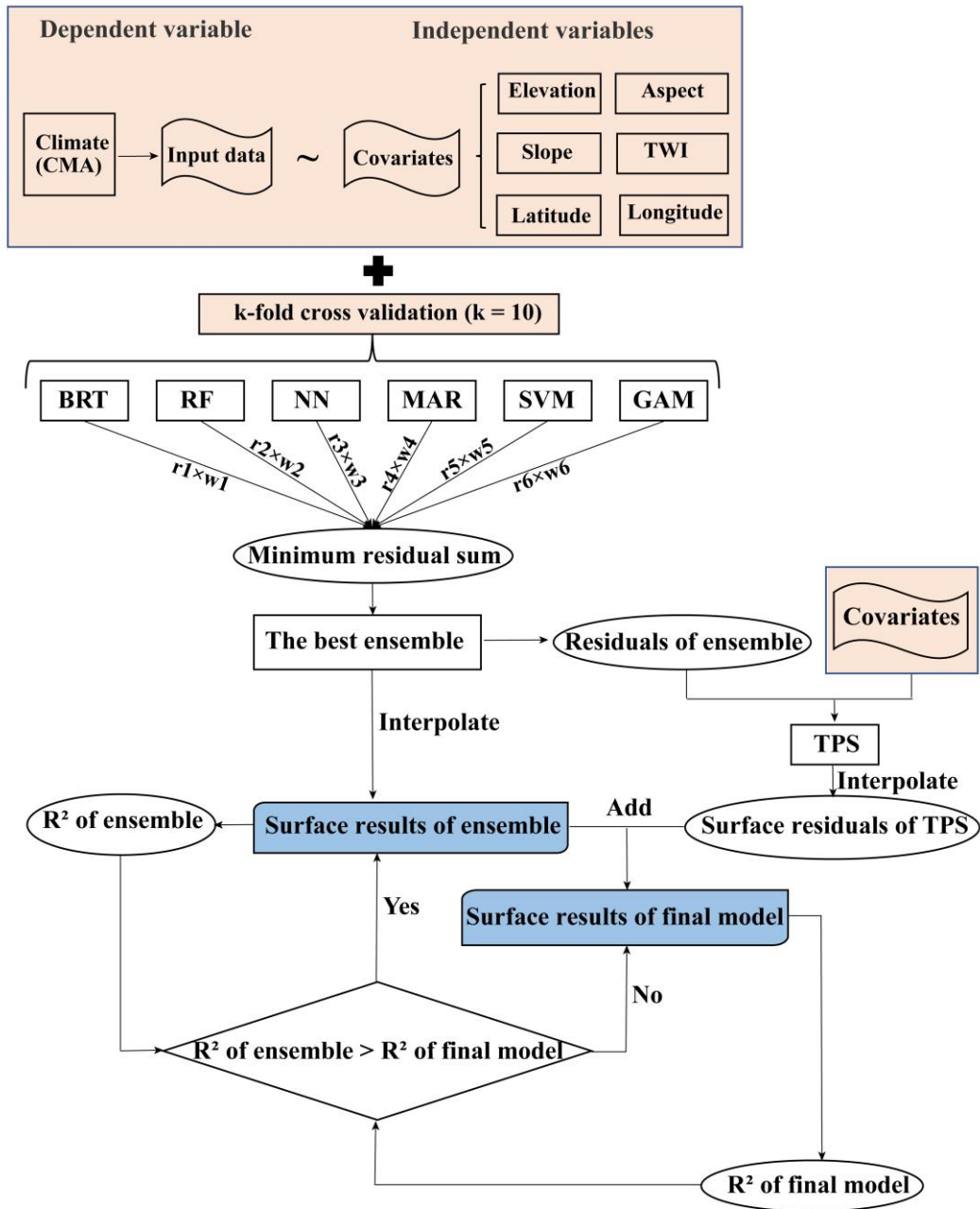


Figure 2. The process of spatial interpolation. The r1 to r6 are the residual error from each algorithm, respectively. The w1 to w6 are the weights of each algorithm, respectively. BRT, RF, NN, MAR, SVR, GAM and TPS are the boosted regression trees, random forests, neural networks, multivariate adaptive regression splines, support vector machines, the generalized additive model and thin-plate-smoothing splines, respectively. R^2 is the coefficient of determination between the estimated and observed values. The TWI is topographic wetness index.

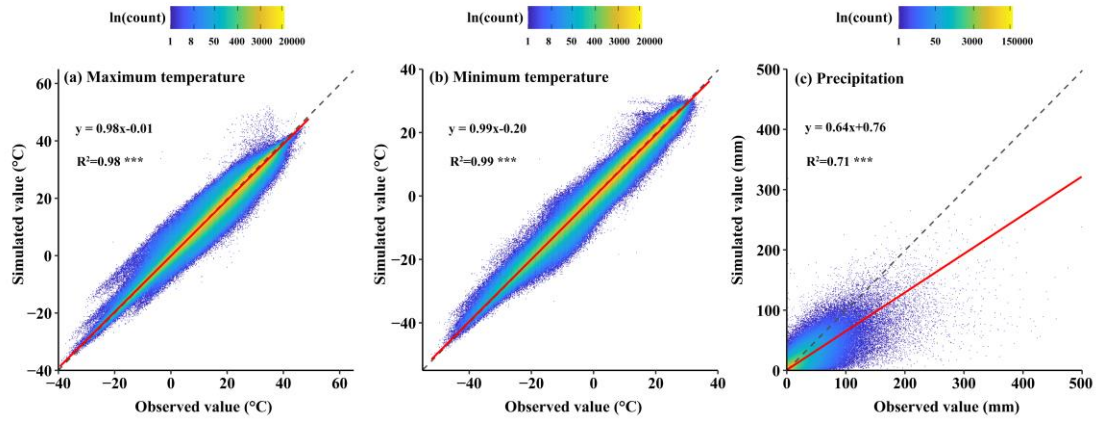


Figure 3. Scatter density plots of daily maximum and minimum temperatures and precipitation between estimated and observed values at meteorological stations were used to test the HRLT dataset. Dashed line is a line with slope 1 and the red line is a fitting between estimated and observed values. R^2 is the coefficient of determination between the estimated and observed values. *** asterisks indicate that the significance of the regression equation between the estimated and observed values was $p < 0.001$.

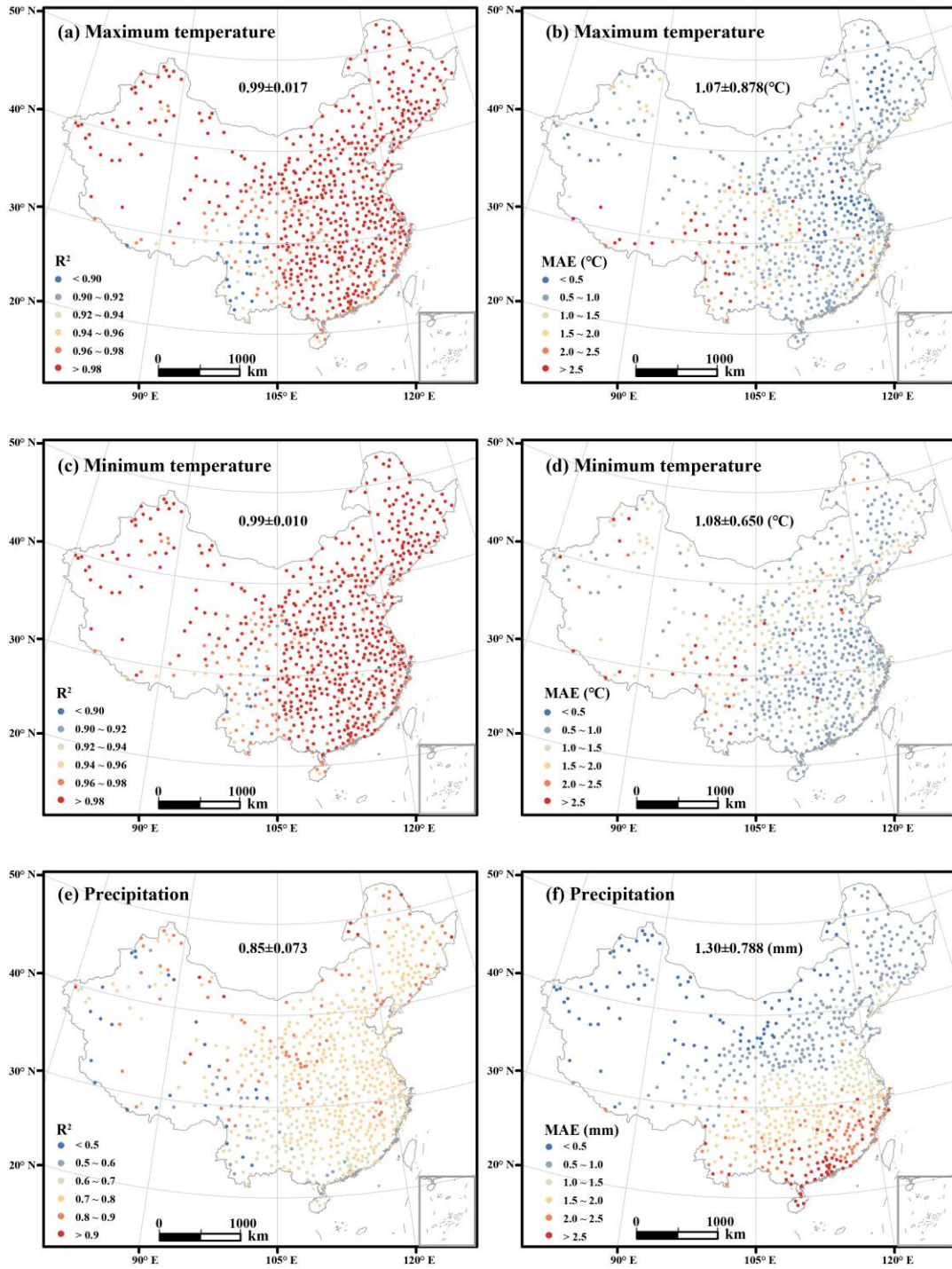


Figure 4. Spatial distribution of R^2 and MAE for daily maximum temperature, minimum temperature, and precipitation between 1961 and 2019. The value before the \pm is the R^2 or MAE mean value and the value after the \pm is the R^2 or MAE standard deviation for all meteorological stations.

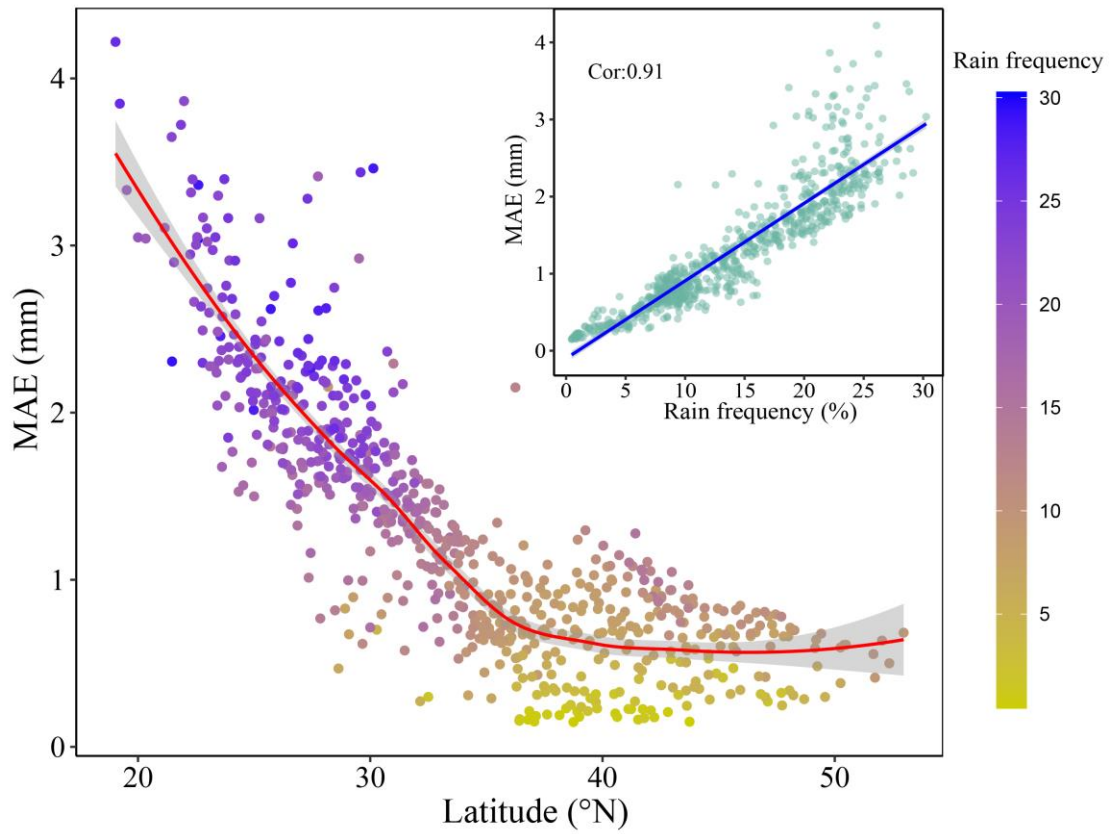


Figure 5. The relationship between latitude and MAE of daily precipitation. Illustration indicates the relationship between rainfall frequency above light rainfall and MAE of daily precipitation. MAE is the mean absolute error, Cor is Pearson's correlation coefficient, Rain frequency is rainfall frequency above light rainfall, which is defined as a daily rainfall from 0 to 4 mm (Alpert et al., 2002)

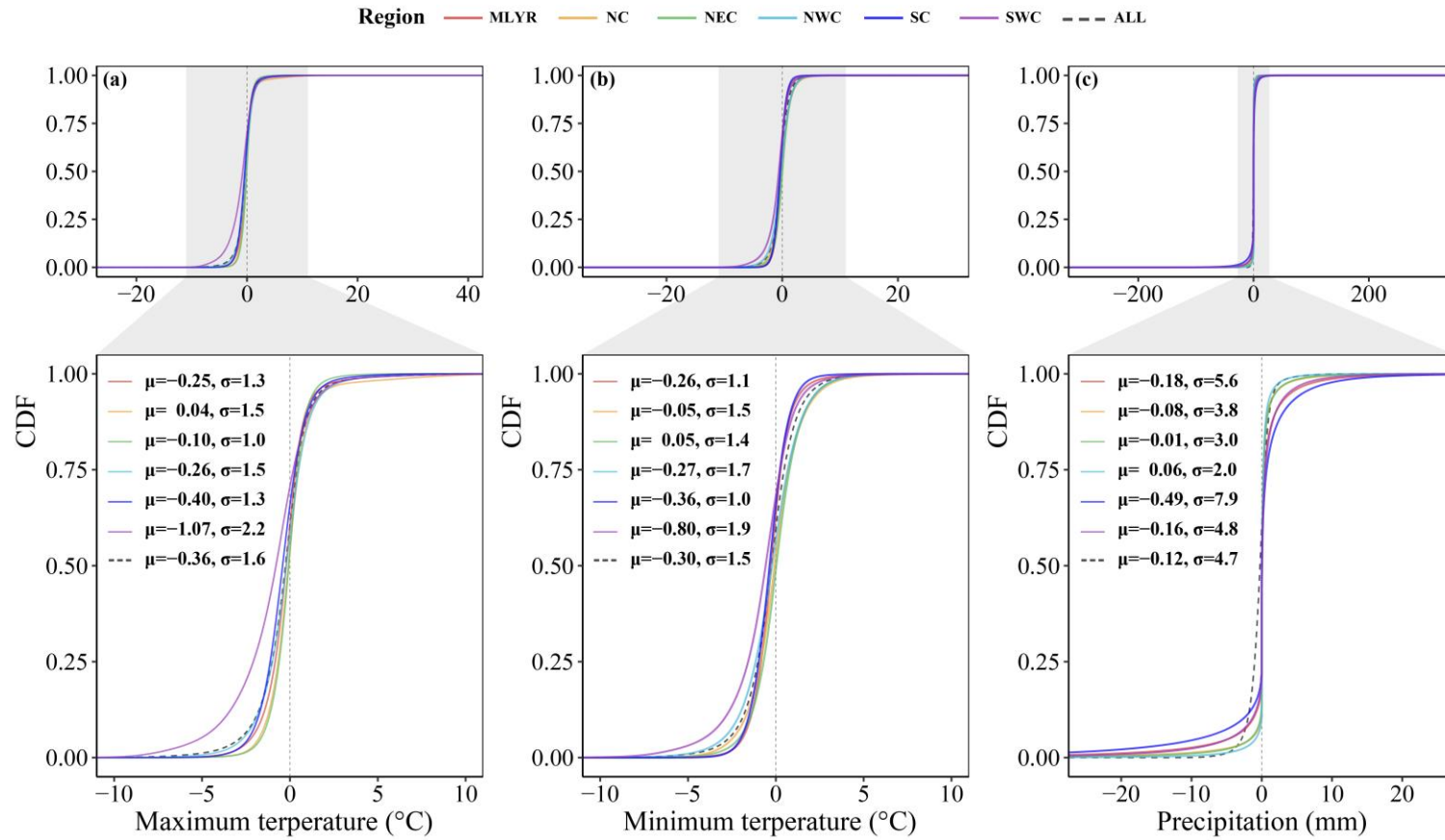


Figure 6. Cumulative distribution functions (CDF) of difference between the estimated and observed values for three variables in all meteorological stations from 1961 to 2020. μ is the mean and σ is the standard deviation. MLYR, NC, NEC, NWC, SC, and SWC are the Middle and Lower reaches of the Yangtze River, North China, Northeast China, Northwest China, South China, and Southwest China, respectively.

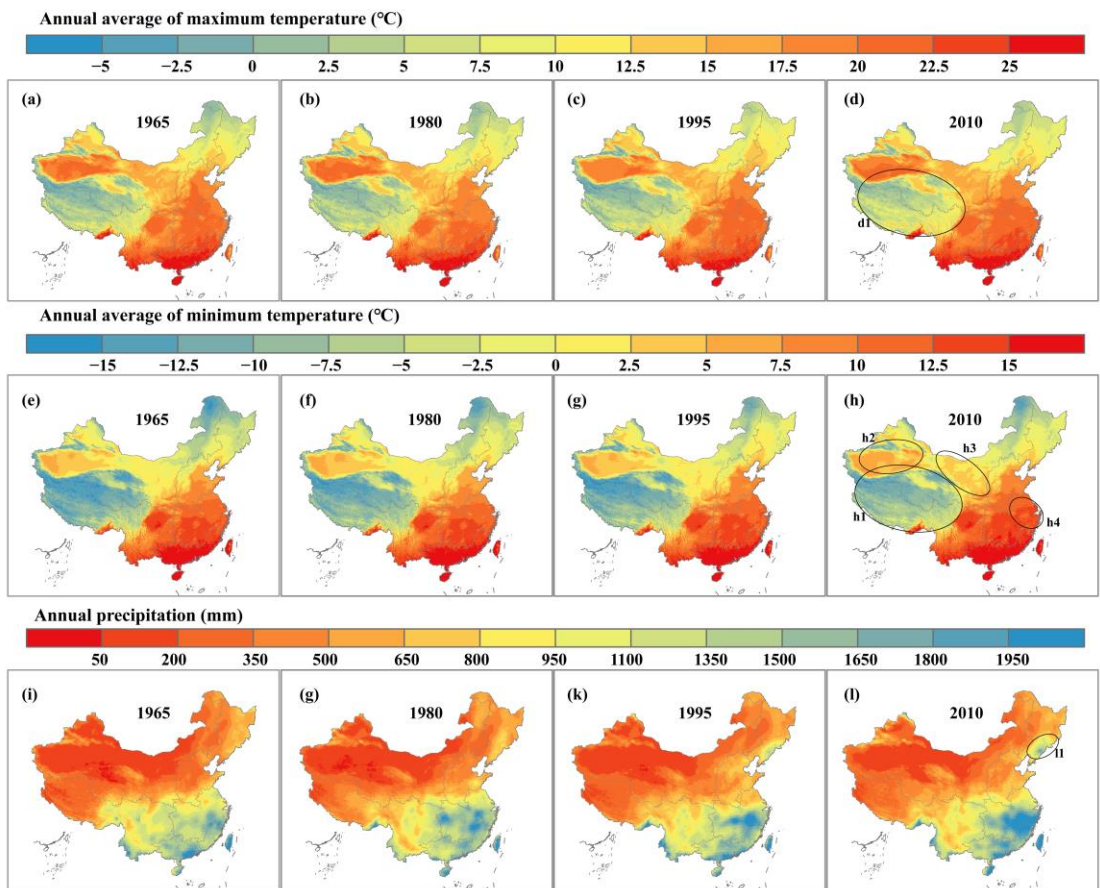


Figure 7. Spatial distributions of annual average values for daily maximum and minimum temperatures, and the spatial distribution of annual precipitation in 1965, 1980, 1990, and 2010. The ellipse regions are where the change is most visible.

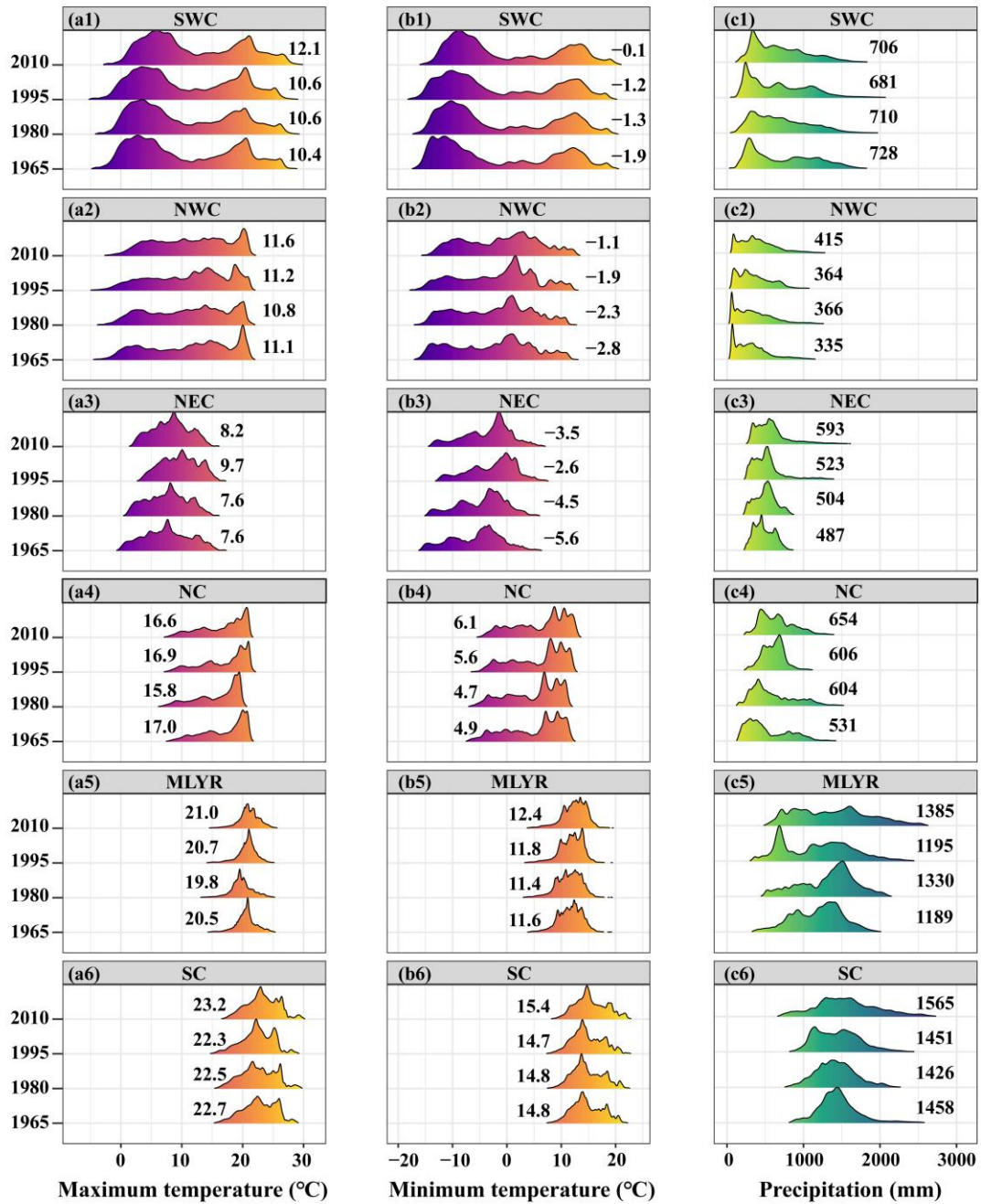


Figure 8. Density distributions of annual average values for daily maximum and minimum temperatures, and annual precipitation across the different regions in 1965, 1980, 1990, and 2010. The value in the illustrations is the mean value.

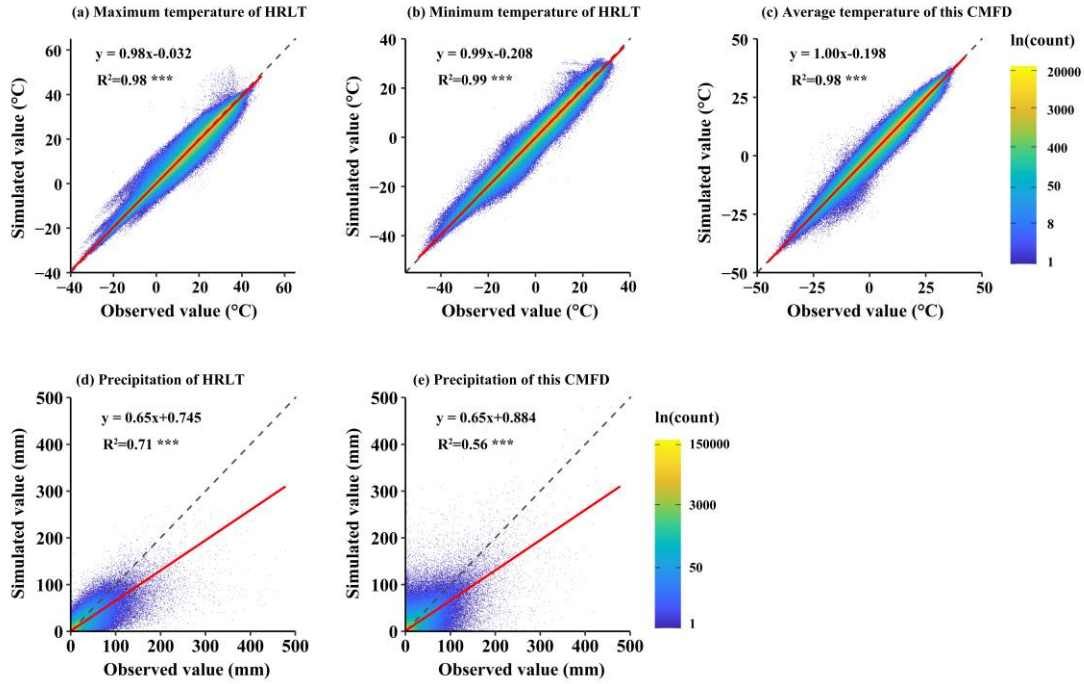


Figure 9. Scatter density plots of daily temperature and precipitation between the estimated and observed values at all meteorological stations (both training sets and testing sets) for the HRLT dataset and the CMFD dataset between 1979 and 2018. The dashed line is a line with slope 1 and the red line is a fitting between the estimated and observed values. R^2 is the coefficient of determination between the estimated and observed values. *** asterisks indicate that the significance of the regression equation between the estimated and observed values was $p < 0.001$.

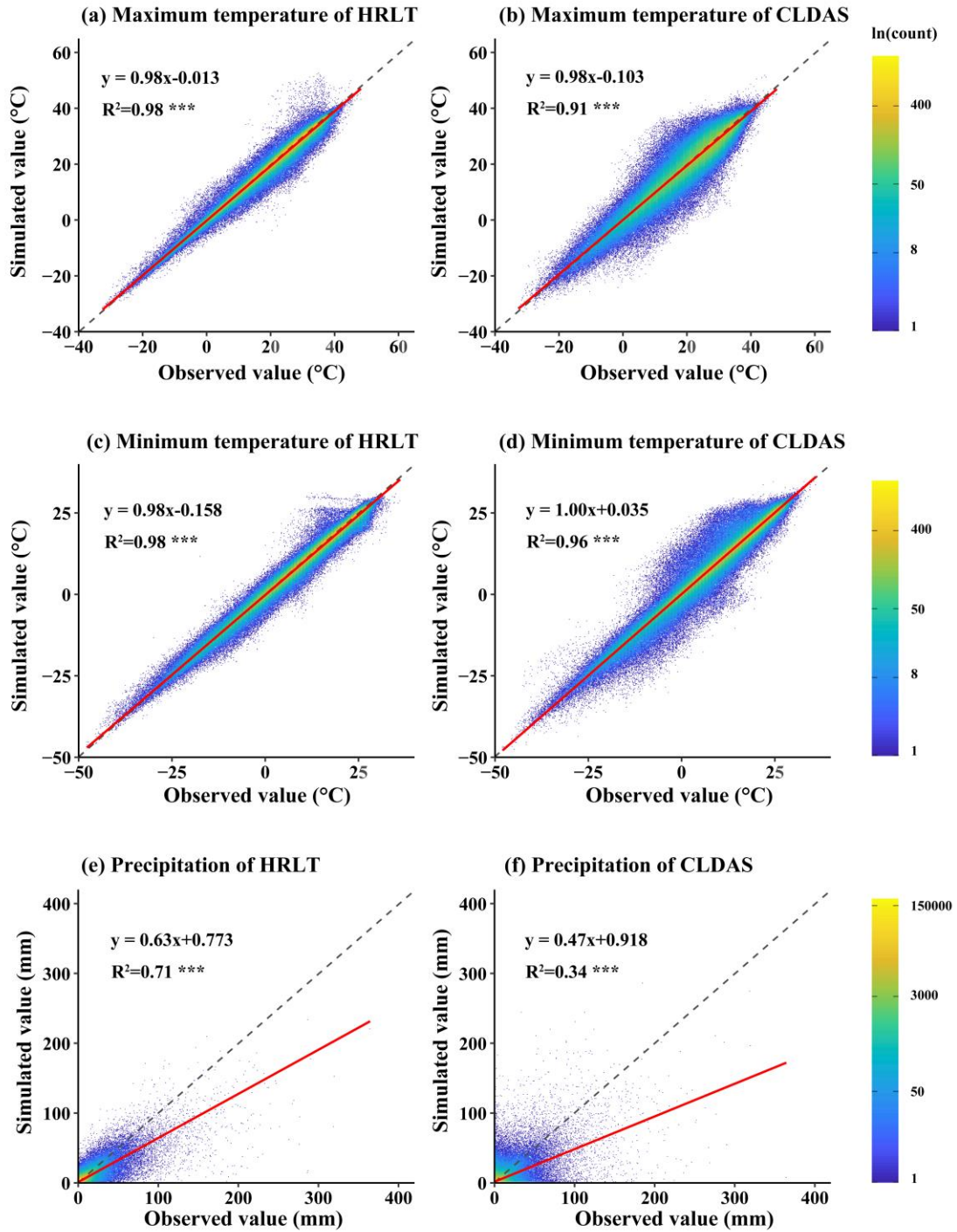


Figure 10. Scatter density plots of daily temperature and precipitation between the estimated and observed values from all meteorological stations (both training sets and testing sets) for our HRLT dataset and the CLDAS dataset between 2017 and 2019. Dashed line is a line with slope 1 and the red line is the fitting between the estimated and observed values. R^2 is the coefficient of determination between the estimated and observed values. *** asterisks indicate that the significance of the regression equation between the estimated and observed values was $p < 0.001$.

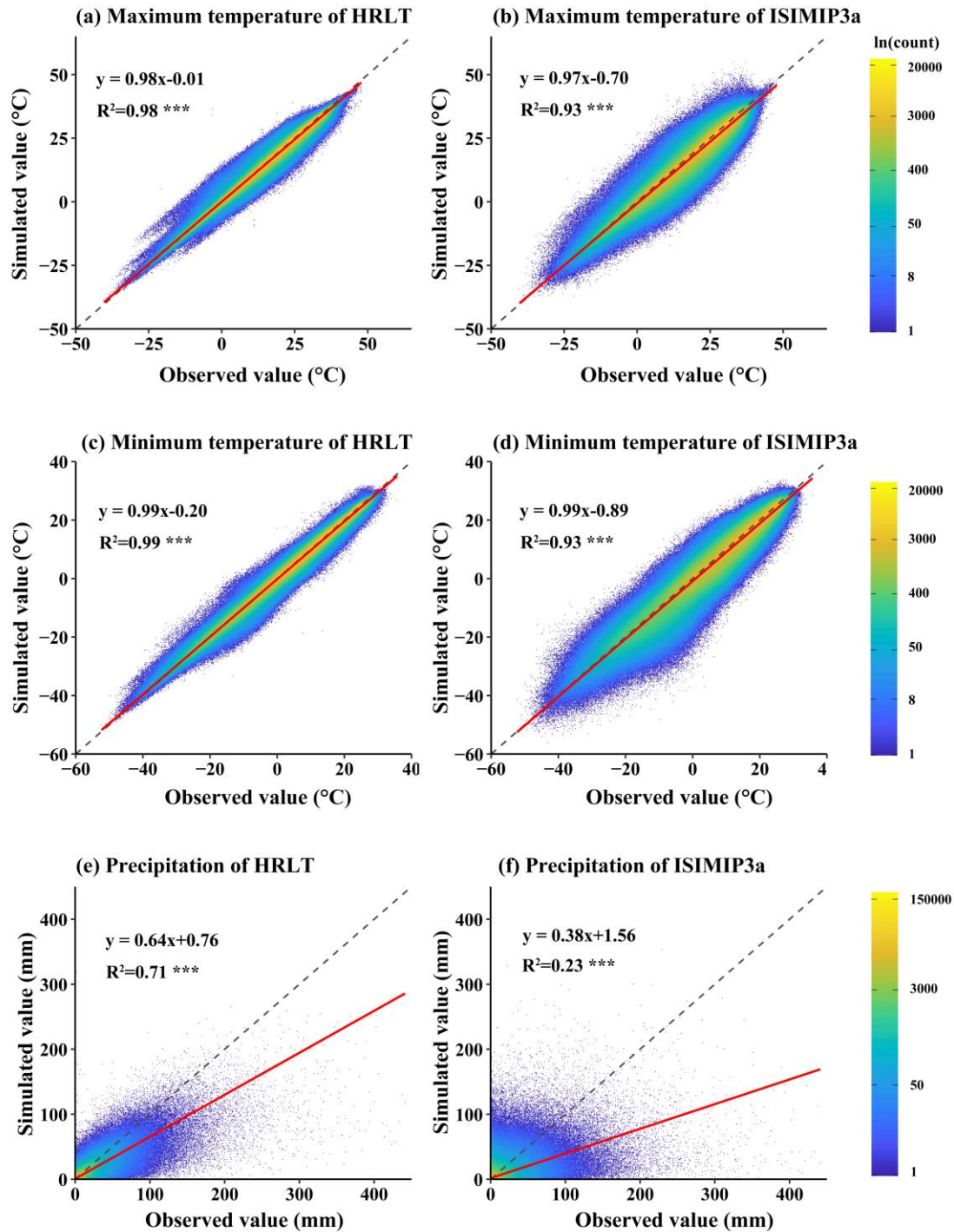


Figure 11. Scatter density plots of daily temperature and precipitation between the estimated and observed values from all meteorological stations (both training sets and testing sets) for our HRLT dataset and the ISIMIP3a dataset between 1961 and 2016. Dashed line is a line with slope 1 and the red line is the fitting between the estimated and observed values. R^2 is the coefficient of determination between the estimated and observed values. *** asterisks indicate that the significance of the regression equation between the estimated and observed values was $p < 0.001$.